



Contents lists available at ScienceDirect

Remote Sensing Applications: Society and Environment

journal homepage: www.elsevier.com/locate/rsase



Multi-band bottom index: A novel approach for coastal environmental monitoring using hyperspectral data

Hiroki Mizuochi ^{*}, Satoshi Tsuchida, Masaru Mizuyama, Satoru Yamamoto, Koki Iwao

Geological Survey of Japan (GSJ), National Institute of Advanced Industrial Science and Technology (AIST), 1-1-1 Higashi, Tsukuba, Ibaraki, Japan



ARTICLE INFO

Keywords:

Coastal monitoring
Satellite hyperspectral sensor
Empirical radiative transfer model
Logarithmic residual method
Hyperion
Ishigaki island

ABSTRACT

Hyperspectral remote sensing has potential for improving shallow-water environmental monitoring, including benthic cover mapping and estimation of bathymetry and water optical properties. Detailed spectral information provided by hyperspectral sensors is particularly required to discriminate benthic covers that have similar spectral patterns (e.g., coral and algae), which cannot be achieved by multispectral sensors with a limited number of wavebands. An important process in such applications is separation of the bottom reflection from the absorption and scattering caused by the water column. Recently, inversion of a semi-analytical radiative transfer model using airborne hyperspectral data has become popular for simultaneous estimation of benthic cover, bathymetry, and water optical properties. However, it requires non-trivial settings and ancillary information, and generally is not user friendly. A cost-effective water-column correction method based on two-band combination has also been popular for multi-band remote sensing; however, it is not suited to hyperspectral data, because of the combinatorial proliferation of many hyperspectral wave bands. To fill the gap between the two approaches, in this paper, a new cost-effective method for water-column correction optimal for hyperspectral data is proposed. The method, called the multi-band bottom index (MBI), incorporates empirical radiative transfer theory and a traditional spectral enhancement technique (i.e., logarithmic residual method). A case study was conducted for the coral reef habitats around Ishigaki Island, using free hyperspectral satellite imagery (Hyperion). The result shows that our MBI approach has more robust performance in the estimation of the water attenuation coefficient than the existing water-column correction approach. The derived MBI map successfully mitigates water-column effects and enhances the spectral pattern of benthic materials. Comparison with in-situ spectra in the literature revealed that the overall spectral pattern of the MBI is reasonable for the benthic categories of coral, seagrass, and sandy bottom. The MBI approach is also promising for application to recently launched hyperspectral satellite sensors, such as HISUI, DESIS, and PRISMA.

1. Introduction

Monitoring of coastal ecosystems is important to evaluate their sustainability under recent climate change conditions (McCarthy et al., 2017). One of the recent issues in coastal ecosystems is coral reef degradation caused by high seawater temperature, acidification, and anthropogenic pollution. These problems degrade the social and ecological benefits of coral reef ecosystems, such as

* Corresponding author.

E-mail address: mizuochi.hiroki@aist.go.jp (H. Mizuochi).

wildlife habitat, seafood, pharmaceuticals, tourism, and shoreline protection (Burke et al., 2011).

Remote sensing through shallow water has been widely used to monitor the coastal environment as a promising counterpart to in-situ fieldwork, due to its advantage of large-scale and cost-effective observation (Hedley et al., 2016; Matthew et al., 2017). Using multispectral and hyperspectral satellite or airborne imagery, researchers have developed techniques to estimate water depth, water quality, and benthic community mapping. Unlike terrestrial remote sensing, remote sensing through shallow water faces complexities, such as mixed signals from bottom reflection and the water column (e.g., Barnes et al., 2013; Arabi et al., 2020). The optical properties of water (i.e., strong absorption in the red to near infrared wavelength region) largely change the apparent spectrum of the target of interest, leading to uncertainty and unsuccessful classification of the bottom materials (e.g., Manessa et al., 2014).

One major approach to separating information on water-column effects and bottom reflection is using analytical radiative transfer simulation. Some studies explicitly simulated the radiative transfer process, including solar incidence, atmospheric absorption and scattering, reflection from the water surface, absorption and scattering by water, reflection from the bottom, and interaction of these phenomena by using shallow-water radiative transfer models (Yamano et al., 2002), such as Hydrolight (Hedley and Mobley, 2019). Inversion techniques with a semi-analytical radiative transfer model (Lee et al., 1998, 1999) using hyperspectral (Lee et al., 2001; Petit et al., 2017; Garcia et al., 2018; Minghelli et al., 2021) or multispectral (Garcia et al., 2020) data are also becoming popular for simultaneous estimation of bathymetry, optical properties of the water, and benthic cover information. However, those approaches require laborious parameter setting and preprocessing, including preparation of the forward model of radiative transfer, a priori information such as object spectra (Manessa et al., 2014), and non-trivial atmospheric correction to retrieve radiometrically accurate reflectance over a coastal area (Gao et al., 2009; Vahtmae and Kutser, 2013). As a result, those methods have usually been implemented with expensive airborne hyperspectral images with abundant in-situ observation data (Petit et al., 2017; Garcia et al., 2018; Minghelli et al., 2021), and have yet to be fully realized through satellite applications (Hedley et al., 2016) in a cost-effective way.

The other major approach is eliminating water-column effects based on an empirical radiative transfer theory and band combination. This approach was first proposed by Lyzenga (1978, 1981) using a two-band ratio of the attenuation coefficient, and various improved algorithms have been developed (Zoffoli et al., 2014). If the optical water properties are assumed to be homogenous over the region of interest, the additive term in the apparent radiance can be subtracted by using sufficiently deep-water pixels (offset correction). Any two-band combination of the offset-corrected radiance can derive a calculable value, sometimes called the “bottom index” (BI) (Matsunaga et al., 2001; Sochea and Sakuno, 2008), which retains bottom reflectance information while eliminating the water-column effect.

The BI approach is usually used for multispectral images such as Landsat (Lyzenga 1981; Andrefouet et al., 2003), IKONOS (Andrefouet et al., 2003; Lyzenga et al., 2006), and the WorldView series (Manessa et al., 2014). Such moderate-to high-resolution images are suited to visualization of the spatial detail of coastal landscapes but not suited to monitoring of spectral information. For example, analysis with a limited number of bands suffers from reduced discrimination of similar spectral patterns for coral and algae (Nadaoka et al., 2004). Monitoring the stress condition of corals (Yamano et al., 2003b) also requires detailed spectral information, which should be provided by hyperspectral imagery.

Cost-effective water-column correction based on empirical radiative transfer, like the BI approach, would be preferable for a wide range of users for processing satellite hyperspectral data. However, applying the existing BI approach to hyperspectral data has two issues. First, selection of two bands from the large number of available bands increases the computational cost and decreases the readability of the results. Because neighboring bands in hyperspectral data generally have high multicollinearity, the derived large BI dataset contains highly duplicated information. Second, because each BI calculation is based only on two bands, uncertainty for each BI value is large in comparison to the case where all effective bands are simultaneously used (Hedley et al., 2016).

To summarize, there is a gap in implementing a cost-effective, operational water-column correction method for satellite hyperspectral images. Filling the gap would enhance the utility of the wide variety of recently emerging hyperspectral satellite sensors, such as the Hyperspectral Image Suite (HISUI; Matsunaga et al., 2018), DLR Earth Sensing Imaging Spectrometer (DESiS; Alonso et al., 2019), and Precursore IperSpettrale della Missione Applicativa (PRISMA; Vangi et al., 2021), as well as the popular free hyperspectral data archive of Hyperion (Ungar et al., 2003), in coastal environment monitoring. In this paper, we propose a new water-column correction method for hyperspectral data, named the multi-band bottom index (MBI) approach. The MBI retains the basic concept of the BI but makes full use of all effective bands simultaneously, and extracts unique spectrum-like information about the bottom material. Therefore, the MBI is more straightforward for hyperspectral data than the existing BI that requires calculation of all possible combinations of band pairs. The MBI process is inspired by a traditional spectral enhancement technique for hyperspectral data called the logarithmic residual method (Green and Craig, 1985; Tsuchida et al., 1993), which is discussed in Section 2.1.

In addition to the proposition of the MBI approach, we also aim to investigate its applicability to real, open (free) satellite hyperspectral data over a coral reef ecosystem. The study site is Ishigaki Island in the Ryukyu Island chain (which includes Okinawa) of southern Japan. Reefs surrounding this island are often reported as a coastal bleaching hot spot by the NOAA Coral Reef Watch (Liu et al., 2014). We performed a comprehensive evaluation, including comparison with the existing BI, physical consistency in estimation of the water attenuation coefficient, and separability of benthic cover using the MBI.

Our interest is to design a calculable value that represents coastal bottom reflectance spectra and excludes or corrects the absorption and scattering effects by the atmosphere and water along the optical path. In Section 2.1, we briefly describe the process of the existing BI approach that enables such a correction with using only two bands, and then expand the concept for hyperspectral data (i.e., the MBI approach). Applicability of the MBI approach was also investigated for coral reef areas near Ishigaki Island (Section 2.2) with Earth Observing-1 (EO-1) Hyperion data (Section 2.3).

2. Materials and methods

We selected images from the EO-1 Hyperion hyperspectral satellite sensor acquired over Ishigaki Island for investigation. The Hyperion image database, which is popular and free, was acquired during satellite operation from 2000 to 2017. Hyperion measured optical radiance for wavelengths of 0.4–2.5 μm at approximately 10-nm intervals, with a 30-m spatial resolution and a 7.5-km swath width (Ungar et al., 2003; Campbell et al., 2013). We also used Landsat 7 ETM + images (USGS, 2018) taken during a similar period, for use as a visualization base map and one data source of visual interpretation.

All the analysis and the algorithm implementation were done by free software: GIS analysis – GRASS GIS 7.4.0; visualization and interpretation – Quantum GIS (QGIS) 2.18.17; and statistical analysis – Python 3.6.9.

2.1. Theory

The top-of-atmosphere radiance observed by a satellite can be separated into the signal from the seafloor coastal bottom reflection and additional terms, including atmospheric path radiance, reflection from the ocean surface, and in-water volume scattering (Kanno and Tanaka, 2012; Manessa et al., 2014). On the basis of a simple water reflectance model (Lyzenga et al., 1978) over a quasi-flat Lambertian bottom, for band b at pixel location i in the satellite image, the top-of-atmosphere radiance $L_{i,b}$ ($\text{W}/\text{m}^2/\text{str}/\mu\text{m}$) can be written as follows:

$$L_{i,b} = E_b R_{i,b} \exp(-k_b f z_i) + L_{0b}, \quad (1)$$

where $R_{i,b}$ is the coastal bottom reflectance that varies for each band and location; k_b is the attenuation coefficient for the ocean (m^{-1}); E_b is a constant that includes the solar irradiance, the round-trip transmittance of the atmosphere and water surface, and the reduction of the radiance due to refraction at the water surface; z_i is the water depth (m), which is independent of the sensor band but sensitive to the pixel location i ; f is a geometric factor to consider the path length through the water, which is assumed to be constant; and L_{0b} is an additional term contributing to the observed radiance, which can be estimated from the pixel values over dark, sufficiently deep water (i.e., pixels free from the bottom reflection). Note that k_b and E_b depend solely on the sensor band (i.e., wavelength), and are assumed to be uniform over the narrow region of interest (i.e., independent from the location i).

On a logarithmic scale, Eq. (1) is transformed to

$$\ln(L_{i,b} - L_{0b}) \equiv \ln D_{i,b} = \ln(E_b R_{i,b}) - k_b f z_i, \quad (2)$$

where $D_{i,b}$ is the offset-corrected radiance. To derive a calculable value that represents coastal bottom reflectance information ($R_{i,b}$), “reference pixels” that have the same reflectance spectrum (i.e., $R_{i,b} = R_b$) but are located over a different water depth are selected from the image. In the existing BI approach, the attenuation coefficient ratio between two bands ($b = p, q$) is determined by

$$\left[\frac{\ln D_{i,p} - \ln(E_p R_p)}{\ln D_{i,q} - \ln(E_q R_q)} \right]_{ref} = \frac{k_p}{k_q} \equiv k_{pq} \quad (3)$$

or

$$[\ln D_{i,p}]_{ref} = k_{pq} [\ln D_{i,q}]_{ref} + [\ln(E_p R_p)]_{ref} - k_{pq} [\ln(E_q R_q)]_{ref}. \quad (4)$$

The operator $[\cdot]_{ref}$ denotes that pixel location i is only within that of the reference pixels. Eq. (4) describes the attenuation coefficient ratio k_{pq} , which can be estimated as the inclination angle of the linear relationship between the offset-corrected radiances of p and q , within reference pixels in a log scale (typically derived from linear regression analysis). The second and the third terms on the right-hand side are intercepts of the linear regression (independent from the pixel location i).

Once k_{pq} is obtained, Eq. (4) is extended for all available pixels:

$$\ln D_{i,p} - k_{pq} \ln D_{i,q} = \ln(E_p R_{i,p}) - k_{pq} \ln(E_q R_{i,q}), \quad (5)$$

or on a linear scale,

$$\frac{D_{i,p}}{D_{i,q}^{k_{pq}}} = \frac{E_p R_{i,p}}{(E_q R_{i,q})^{k_{pq}}}. \quad (6)$$

The left-hand side is the calculable value from the satellite image, and the right-hand side represents bottom reflectance information. The calculable value is the BI for bands p and q , which can be used to classify coastal benthic covers and materials without the water-column effect.

Our MBI expands this concept for hyperspectral images with more flexibility, through simultaneous consideration of all effective band information. The specific MBI procedure was inspired by a traditional technique for spectral enhancement called the logarithmic residual method (Green et al., 1985; Tsuchida et al., 1993). The MBI approach estimates a standardized attenuation coefficient instead of the k_{pq} in the BI approach, and derives calculable values for each band that incorporates bottom reflectance information (i.e., arbitrary selection of two bands is not necessary).

When the arithmetic mean of Eq. (2) for pixel location i is subtracted from each side of the original Eq. (2), the constant term E_b is canceled out as follows:

$$\ln D_{i,b} - \frac{1}{m} \sum_i \ln D_{i,b} - \left(\ln R_{i,b} - \frac{1}{m} \sum_i \ln R_{i,b} \right) = -k_b f \left(z_i - \frac{1}{m} \sum_i z_i \right), \quad (7)$$

where m is the total number of pixels ($i = 1, 2, \dots, m$). Further, when the arithmetic mean of Eq. (7) for band b is divided into each side of Eq. (7), location-dependent term z_i is canceled out:

$$\frac{\ln D_{i,b} - \frac{1}{m} \sum_i \ln D_{i,b} - \left(\ln R_{i,b} - \frac{1}{m} \sum_i \ln R_{i,b} \right)}{\frac{1}{n} \sum_b \left(\ln D_{i,b} - \frac{1}{m} \sum_i \ln D_{i,b} \right) - \frac{1}{n} \sum_b \left(\ln R_{i,b} - \frac{1}{m} \sum_i \ln R_{i,b} \right)} = \frac{k_b}{\frac{1}{n} \sum_b k_b} \equiv k'_b, \quad (8)$$

where n is the number of used bands. Eq. (8) defines the standardized attenuation coefficient k'_b , which is the attenuation coefficient for each band, scaled by the arithmetic mean of all band coefficients. By focusing only on the reference pixels, it can be further simplified:

$$\left[\ln D_{i,b} - \frac{1}{m_r} \sum_i \ln D_{i,b} \right]_{ref} \Bigg/ \left[\frac{1}{n} \sum_b \left[\ln D_{i,b} - \frac{1}{m_r} \sum_i \ln D_{i,b} \right]_{ref} \right] = k'_b. \quad (9)$$

Note that the pixel location i can only be within the range of reference pixels ($i = 1, 2, \dots, m_r$). The left-hand side is calculable, so that we can obtain k'_b using the offset-corrected radiance value over the range of reference pixels. k'_b can be calculated for each reference pixel, resulting in a total of m_r outputs from Eq. (9). Given the abovementioned assumption that k_b (relating to optical water properties) is uniform over the narrow region of interest, it is independent of the pixel location i , and all the k'_b values are expected to be the same. However, a fluctuation in the series of k'_b probably persists due to spatial heterogeneity and other uncertainties in the Hyperion data or the algorithm. Therefore, the arithmetic mean of all k'_b values is used hereafter as the best available k'_b estimate, and the standard error is used as the uncertainty in k'_b .

After obtaining k'_b , a calculable value that represents bottom reflectance information can be derived by arranging Eq. (8) for all available pixels over the shallow-water area:

$$\begin{aligned} & \ln D_{i,b} - \frac{1}{m} \sum_i \ln D_{i,b} - \frac{k'_b}{n} \sum_b \left(\ln D_{i,b} - \frac{1}{m} \sum_i \ln D_{i,b} \right) \\ &= \ln R_{i,b} - \frac{1}{m} \sum_i \ln R_{i,b} - \frac{k'_b}{n} \sum_b \left(\ln R_{i,b} - \frac{1}{m} \sum_i \ln R_{i,b} \right). \end{aligned} \quad (10)$$

Alternatively, on a linear scale, the arithmetic mean is replaced by a geometric mean:

$$\left[\frac{D_{i,b}}{\left(\prod_i D_{i,b} \right)^{\frac{1}{m}}} \right] \Bigg/ \left[\prod_b \frac{D_{i,b}}{\left(\prod_i D_{i,b} \right)^{\frac{1}{m}}} \right]^{\frac{k'_b}{n}} = \left[\frac{R_{i,b}}{\left(\prod_i R_{i,b} \right)^{\frac{1}{m}}} \right] \Bigg/ \left[\prod_b \frac{R_{i,b}}{\left(\prod_i R_{i,b} \right)^{\frac{1}{m}}} \right]^{\frac{k'_b}{n}}. \quad (11)$$

The left-hand side is the calculable value from the satellite image, and the right-hand side represents bottom reflectance information. The calculable value defines our proposed MBI.

Unlike the BI, the MBI is calculable for each band, and it reflects all band reflectance information. Mathematically, the MBI describes the reflectance normalized by the geometric mean of reflectance for pixel location i , further normalized by the geometric mean of that value for band b with weighting factor k'_b . Although it is not a pure physical spectrum of reflectance, MBI spectrum reflects the spectral features of benthic covers and materials, and is expected to be useful for coastal monitoring.

2.2. Study site

The study site, Ishigaki Island, is surrounded by a typical fringing coral reef of several hundred to a thousand meters in width (Hasegawa and Yamano, 2004). Reflecting the ocean wave energy environment, the coast facing the Pacific Ocean consists of well-developed reef, whereas the reef along the opposite coast is poorly formed and discontinuous (Hasegawa and Yamano, 2004; Yamano et al., 2003a). The coral reef in Ishigaki Island has experienced bleaching events repeatedly (Yamano and Tamura, 2004) and is designated as a coral reef monitoring site by the Ministry of the Environment, Japan (MOEJ). MOEJ has conducted field surveys of benthic cover around Ishigaki Island several times (MOEJ, 1991; 2018), and publicly distributes the results through a GIS web-site

Table 1
Coordinates of the three test sites.

Site	Latitude (UTM51/geographic)	Longitude (UTM51/geographic)
Site 1	2713500-2718000/24.5301N-24.5704N	627000-631500/124.2538E-124.2986E
Site 2	2690000-2694500/24.3185N-24.3588N	620200-624700/124.1847E-124.2294E
Site 3	2697000-2701500/24.3813N-24.4215N	625500-630000/124.2375E-124.2823E

(http://www.biodic.go.jp/trialSystem/top_en.html). We used this site as the primary data source to interpret benthic cover types at the study site.

To investigate the effect of differences in location and landscape on the estimation of the water attenuation coefficient and MBI, three regions of interest were selected (Table 1; Fig. 1).

Site 1, located on the northwest coast (Kuura), is characterized by an undeveloped reef crest and a mixture of sparse seagrass and sparse coral on a sandy bottom. This environment creates relatively homogeneous pixels with a variety of water depths, which may be useful for estimation of the attenuation coefficient. Site 2, located on the south coast (Miyara), includes developed reef crests with some gaps, the Miyara River estuary, and relatively large areas of sandy or silty bottom. MOEJ GIS data indicate that algae covers the eastern shoreline, whereas seagrass covers the western shoreline at the site. Site 3, located on the southeast coast (Shiraho), is famous for its rich coral community and has often been targeted by coral remote sensing research (e.g., Kayanne et al., 2002; Andrefouet et al., 2003). The well-developed coral reef along the coast forms zonal structures of seagrass, sandy bottom, and coral communities within the reef flat (i.e., shallow lagoon), where the range of water depth is limited. At the reef crest and its underlying reef substrate, broken waves can be observed as points with high brightness on the satellite image.

For estimation of the water attenuation coefficient, homogeneous reference pixels (preferably with a wide variety of water depth), and sufficiently deep-water pixels should be determined. For each site, 20 reference and 20 deep-water pixels were determined, by visual interpretation of Hyperion data (details are provided in Section 2.3) with the help of MOEJ survey data and Google Earth images. For site 3, we did not sample the deep-water pixels because the nearest open sea area is on the edge of the Hyperion scene (see the left image in Fig. 1), but we instead used common deep-water pixels from site 2, which also faces the Pacific Ocean and is only 10 km distant from site 3.

Furthermore, land and deep-water areas were masked out by polygons manually created using QGIS software, for calculation and visualization of the MBI. This helps the MBI to focus only on the shallow-water benthic cover within the reef flat, and exclude terrestrial land cover and noise-level signals over deep water.

2.3. Case study with a real hyperspectral satellite image

A UTM-projected Hyperion scene with little cloud contamination and sun glint effect, taken on 2001/10/02, was downloaded through the USGS EarthExplorer website (<https://earthexplorer.usgs.gov>). Among the 224 total Hyperion bands, only the visible and near-infrared spectral regions were used, and uncalibrated bands (Bands 1–7) were excluded. For the remaining bands (Bands 8–57), the original digital number was converted into radiance ($\text{W}/\text{m}^2/\text{str}/\mu\text{m}$) by dividing by a scaling factor of 40.

Although the Hyperion scene was the terrain-corrected (i.e., L1T) product, we found a substantial mis-registration in comparison

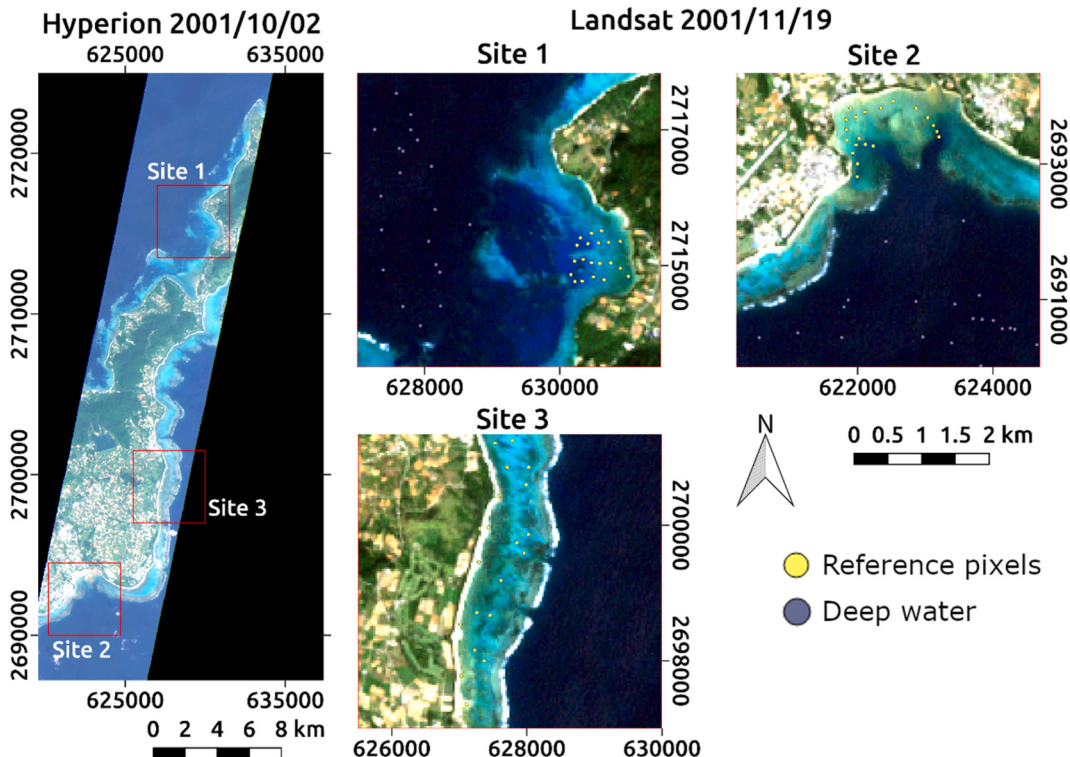


Fig. 1. (left) Satellite image (Hyperion true color) over Ishigaki Island and (right) detailed images of the three test site locations (Landsat true color). Coordinates are the UTM zone 51 projection on the WGS84 datum. For each test site, the distribution of reference pixels and deep-water pixels is shown by yellow and purple points, respectively. (For interpretation of the references to color in this figure legend, the reader is referred to the Web version of this article.)

with the other satellite data sources (i.e., Landsat and Google Earth). To mitigate the geolocation error of the scene, we took 20 ground control points and overlaid a Hyperion true color image (assigning Bands 15, 21, and 30 as blue, green, and red channels, respectively) on a Google Earth image using the QGIS software. The selection of these three bands is based on the correspondence to the band wavelength of the other well-known freely available multispectral sensor data (Landsat and Sentinel 2) that provide moderate spatial resolution (i.e., comparable to that of Hyperion). For example, the center wavelength of the Sentinel 2 blue band is 493 nm, closest to the Hyperion Band 15 (498.04 nm), which is also within the spectral range of the ETM + blue band (450–520 nm). Similarly, the green band of Sentinel 2 (560 nm) and ETM+ (520–600 nm) would correspond to Hyperion Band 21 (559.09 nm). Strictly speaking, the red band should be Hyperion Band 31 (660.85 nm) for correspondence with the red band of Sentinel 2 (665 nm). However, Band 31 was out of the “effective band” range (as discussed below), and thus Band 30 (650.67 nm) was used instead, which is in the range of the ETM + red band (630–660 nm).

Then we applied georectification of all the Hyperion band images by second-order polynomial transformation with nearest neighbor resampling. Moreover, inter-band coregistration was ensured with reference to Band 15 of the Hyperion image using the phase-only correlation method (Miura et al., 2012).

After the preprocessing, the Hyperion bands substantially suffering from water absorption were further excluded, and only bands showing a sufficient signal even in the shallow-water area (hereafter “effective bands”) were used in our algorithm implementation. To this end, we statistically checked the radiance difference between the reference and deep-water pixels. We defined the effective band as a band where the maximum radiance among deep water pixels does not exceed the minimum radiance among reference pixels. The reference pixels taken from shallow-water areas should contain additional signals from the bottom, and thus if any reference pixels indicate values lower than those of deep water, the signal from the bottom in the band is assumed to be at noise level. The criteria extracted Bands 9–30 and Bands 33–34 as the effective bands for site 1 (Fig. 2), and similarly, Bands 9–55 for site 2 and Bands 9–49 for site 3 (figures not shown). Taking the common continuous part, we decided to use Bands 9–30 for the algorithm implementation (we discuss the effect of band selection in Sections 3 and 4).

With the effective bands, the standardized water attenuation coefficient k_b' was calculated for each site, using the reference and deep-water pixels. Three representative bands used for true-color visualization (Bands 15, 21, and 30) were examined and compared with the existing BI approach in their performance for reasonable estimation of the attenuation coefficient.

After k_b' was estimated, the MBI was calculated for all available pixels in the reef flat, to make a MBI map for each site. In addition, the MBI spectra were investigated for each specific benthic cover type. To this end, we collected ground reference data for several benthic cover types. Collecting the reference data for past benthic cover is not a straightforward task. We can rely on the nearest MOEJ in-situ surveyance (MOEJ, 1991) to some extent; however, there may be a change in benthic cover from the survey period (1989–1992) to the Hyperion overpass period (2001). Therefore, we also referred to the recent MOEJ in-situ survey (MOEJ, 2018), the other optical satellite image (Landsat) taken in 2001, and time-series Google Earth images to extract homogeneous, pseudo-invariant points. Based on visual interpretation of all the above data sources, the 10 proxy reference points for four or five benthic cover categories (i.e., coral, seagrass, reef substrate, and sandy bottom for sites 1 and 3, and algae in addition to the previous four categories for site 2) were

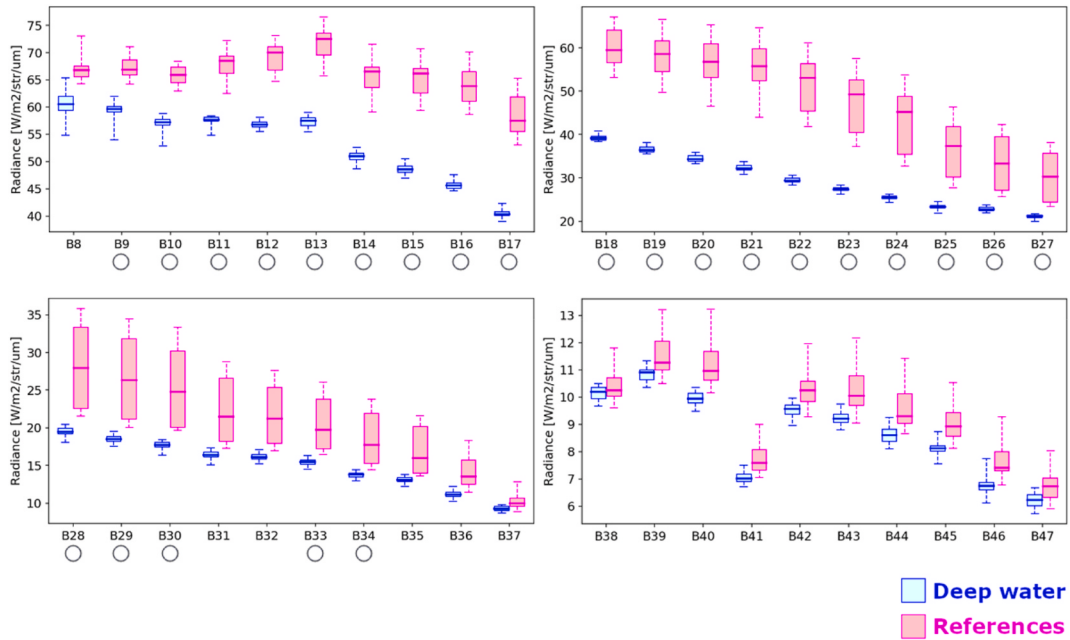


Fig. 2. Boxplots of the radiance in deep-water pixels (blue) and reference pixels (pink), for each Hyperion band (Bands 8–47). Band numbers with circles under them indicate the “effective bands” (see Section 2.3 for the definition). The correspondence between Hyperion band numbers and wavelengths is summarized in the Appendix. (For interpretation of the references to color in this figure legend, the reader is referred to the Web version of this article.)

collected for each test site.

3. Results

Using the two stages of our approach, we provide results for estimation of the water attenuation coefficient using the reference pixels (Section 3.1), and calculate the MBI for all available pixels over shallow-water areas (Section 3.2).

3.1. Estimation of water attenuation coefficient

First, we show the results for the existing BI approach as a benchmark. Fig. 3 and Table 2 show the estimation of water attenuation coefficients for three representative bands (Bands 15, 21, and 30). Scatter plots of the offset-corrected radiance in a log scale, $\ln D_{i,b}$, did not necessarily show good correlation between band pairs. Site 2 showed a high correlation coefficient (>0.9) for all band pairs, and the derived slope of the perpendicular regression line (i.e., ratio of the attenuation coefficients for the two bands) seemed to be reasonable for water absorption: the coefficient in Band 15 (k_{15}) was less than k_{21} , k_{21} was far less than k_{30} , and consequently k_{30} was substantially (i.e., 2.5 times) high in comparison to k_{15} . The product of the first two ratios, $k_{15}/k_{21} \times k_{21}/k_{30} = 0.413$, was also consistent with the reciprocal of the last ratio, $1/(k_{30}/k_{15}) = 0.403$.

The other two sites suffered from low correlation between bands, particularly for blue (Band 15) versus red (Band 30) pairs. Ratio k_{30}/k_{15} at site 1 was close to zero, meaning that water attenuation of the red band was much smaller than that of the blue band, which was not consistent with the results from the other ratios. Ratio k_{30}/k_{15} at site 3 was likely to have been too high. The product of the first two ratios, $k_{15}/k_{21} \times k_{21}/k_{30} = 0.528$, was not consistent with the reciprocal of the last ratio, $1/(k_{30}/k_{15}) = 0.174$, and thus the estimation likely contains a large uncertainty.

Apart from the BI result, our MBI approach enabled simultaneous estimation of the standardized attenuation coefficients from Bands 9–30 (Fig. 4). Attenuation coefficients for pure water and pure seawater from the literature (Hale and Querry, 1973; Smith and Baker, 1978) are also drawn for reference. Note that all values were scaled by the number of effective bands (n), so that summation of k_b/n for all the effective bands can be 1.0. The estimated k_b/n values using Bands 9–30 were well consistent with the overall spectral pattern of pure water and pure seawater for all sites (Fig. 4a, e, f): a very small value for blue to green wavelength regions

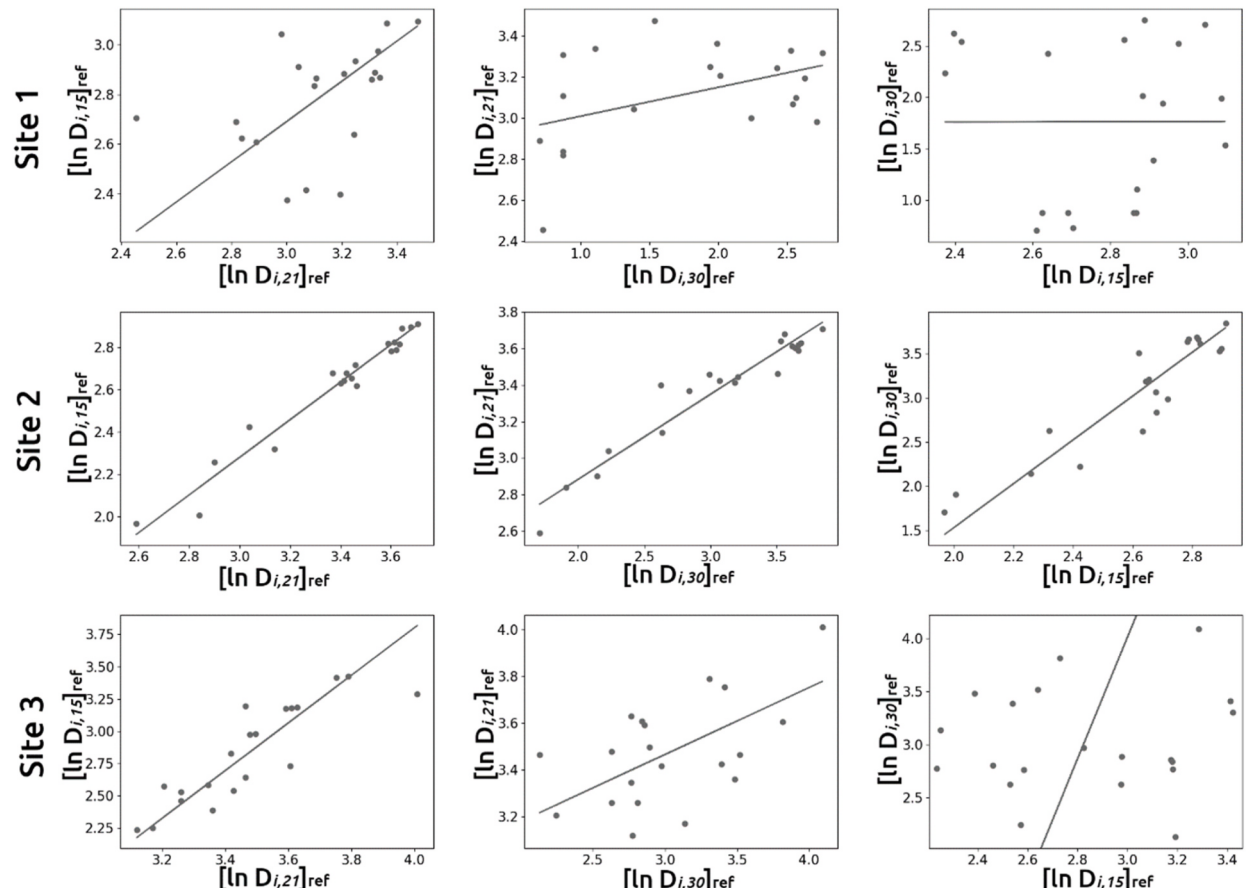


Fig. 3. Scatterplots of offset-corrected radiance in log scale ($\ln D_{i,b}$) between all pairs of Bands 15, 21, and 30. One sample point corresponds to one reference pixel, and the lines are perpendicular regression results. Top row: site 1; middle row: site 2; bottom row: site 3. Right column: Band 21 versus Band 15; center column: Band 30 versus Band 21; left column: Band 15 versus Band 30.

Table 2

Estimation of the attenuation coefficient by the existing BI method for the three test sites. Slope and intercept of the perpendicular regression line (see Fig. 3), and correlation coefficient between the bands are shown. The slope corresponds to the ratio of the attenuation coefficient between two bands.

Ratio	Slope	Intercept	Correlation coefficient
Site 1			
k_{15}/k_{21}	0.811	0.258	0.442
k_{21}/k_{30}	0.141	2.867	0.414
k_{30}/k_{15}	0.008	1.742	-0.024
Site 2			
k_{15}/k_{21}	0.887	-0.381	0.979
k_{21}/k_{30}	0.466	1.950	0.962
k_{30}/k_{15}	2.481	-3.427	0.927
Site 3			
k_{15}/k_{21}	1.846	-3.583	0.868
k_{21}/k_{30}	0.286	2.608	0.545
k_{30}/k_{15}	5.735	-13.195	0.091

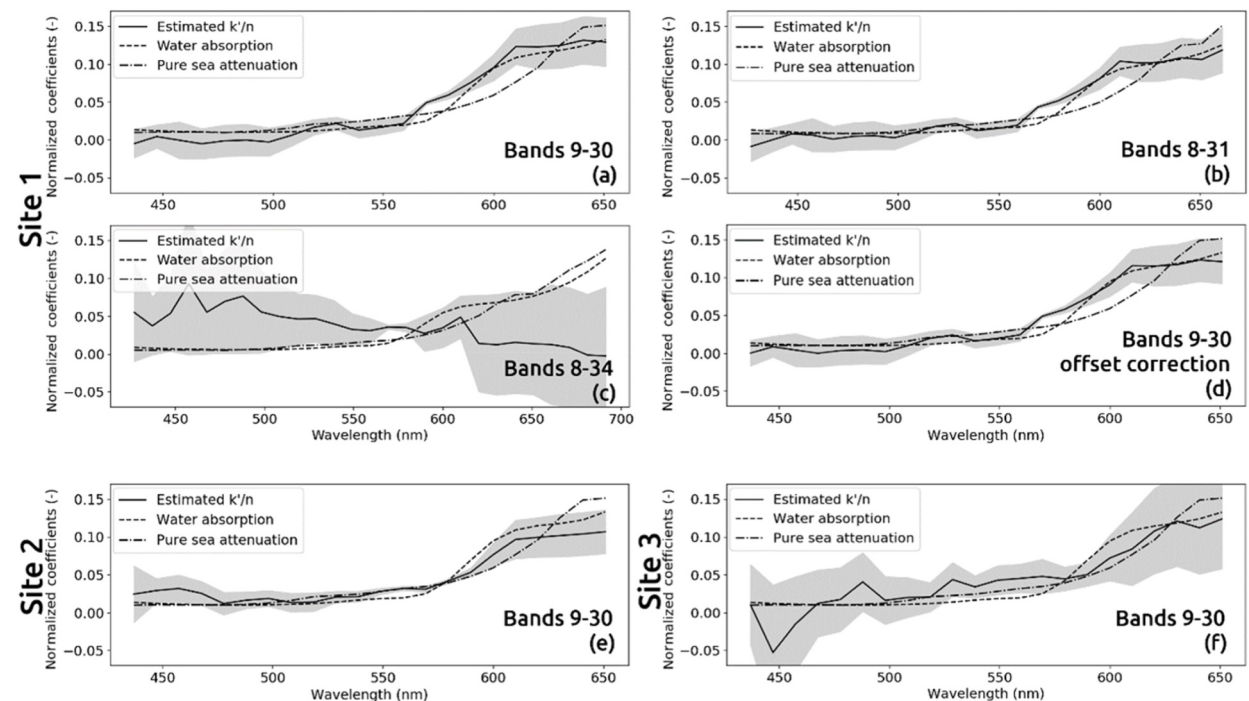


Fig. 4. Standardized attenuation coefficient k_b' (scaled by n , the number of bands) estimated by the MBI (solid lines). The equivalent values of pure water (dashed lines; Hale and Querry, 1973) and pure seawater (dash-dotted lines; Smith and Baker 1978) are also drawn. Grey areas indicate the standard error of the estimation ($m_r = 20$). (a–c) show the effect of band selection at site 1. (d) is the offset-corrected result of (a). (e) and (f) show the results at sites 2 and 3, respectively.

Table 3

Comparison of the standardized attenuation coefficient only for the representative bands (Bands 15, 21, and 30) among MBI and BI estimates, and from the literature (Hale and Querry, 1973; Smith and Baker, 1978).

Method	k_{15}'	k_{21}'	k_{30}'
Site 1			
MBI estimation	0.043	0.495	2.462
BI estimation	1.339	0.337	0.024
Site 2			
MBI estimation	0.356	0.610	2.035
BI estimation	0.651	0.744	1.605
Site 3			
MBI estimation	0.792	0.767	1.441
BI estimation	0.411	0.474	2.055
References			
Pure water	0.192	0.360	2.449
Pure seawater	0.194	0.487	2.318

(approximately 400–550 nm), a rapid increase around 600 nm, and a high value in the red wavelength region (~650 nm). For site 1, except for the slightly negative values in the blue region and slightly larger values around 570 nm, the overall shape of the attenuation coefficient was quite consistent with those in the references, revealing the advantage of the MBI over BI. For site 2, k_b'/n was slightly high at the shortest wavelength region (450 nm). The site 3 result had the largest standard error in the estimation, with several spikes at

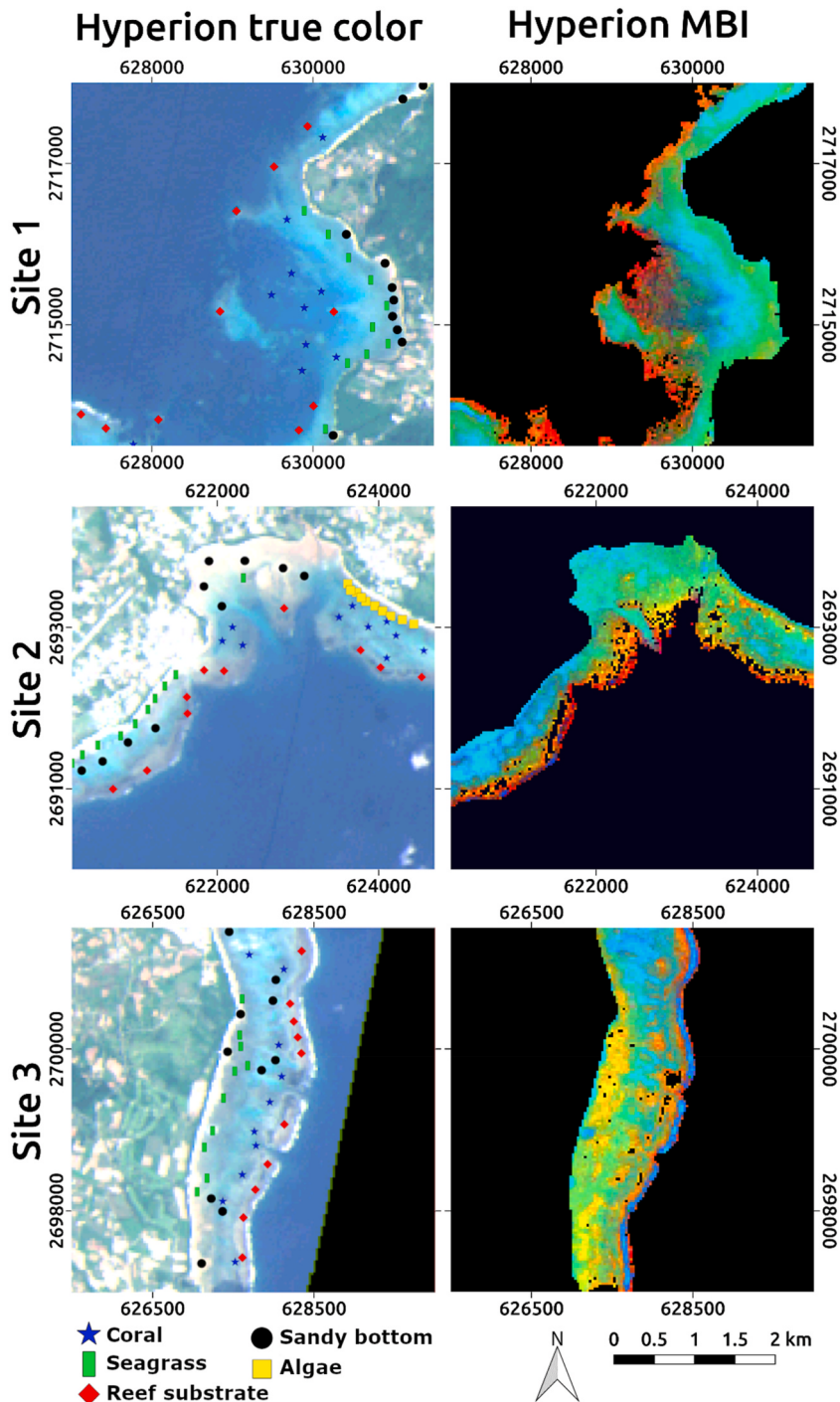


Fig. 5. Comparison between (left) Hyperion true color image (red: Band 30; green: Band 21; blue: Band 15) and (right) MBI image with assigned corresponding color bands for the three test sites. The black pixels in the MBI images indicate null values, due to masking by land or deep sea or a negative value of $D_{i,b}$. Benthic cover reference points are shown on the true color images with colored symbols. Interpretation of the categories was based on the marine biotic survey (coral reef survey) in the 4th national survey on the natural environment (Ministry of the Environment, Biodiversity Center of Japan). (For interpretation of the references to color in this figure legend, the reader is referred to the Web version of this article.)

around 450 nm, 480 nm, and 530 nm, and some negative values around the blue wavelength region.

Table 3 compares k_b'/n values extracted by the BI and MBI for the representative three bands (Bands 15, 21, and 30 newly standardized with $n = 3$). The algebra of the result from the BI approach, such as $k_{15}'/n = k_{15}/(k_{15} + k_{21} + k_{30}) = 1/(1 + k_{21}/k_{15} + k_{30}/k_{15})$, showed a physically implausible result for site 1: the largest attenuation occurred in the blue band, and the smallest attenuation occurred in the red band. At site 2, coefficients estimated by the BI varied over a smaller range than those estimated by the MBI. When compared with the reference water coefficients, results from the MBI are more realistic. Conversely, at site 3, the BI seemed to be better than the MBI, confirming a somewhat uncertain result for the MBI at site 3, as shown in Fig. 4f. Nevertheless, the MBI showed greater overall robustness at different sites than the BI, which relies only on two-band correlation. In **Table 3**, the RMSE for k_b' estimated from the MBI over all the sites was 0.453 against pure water and 0.392 against pure seawater, whereas that from the BI was 0.971 against pure water and 0.913 against pure seawater.

Selection of the effective bands was important for successful estimation of k_b' (Fig. 4a–c). Both results from Bands 9–30 and Bands 8–31 showed good consistency with the references; however, when longer-wavelength bands (Bands 8–34) were added, the result became unstable and highly uncertain. This result supports the validity of the band selection criteria (Section 2.3).

For site 1, several slightly negative values were observed around the blue wavelength regions, due to the inevitable uncertainty in estimation with the limited number of reference pixels. Such values should hamper further processing for MBI calculation. To eliminate such values while keeping the spectral shape of the estimated k_b'/n , we added a common offset to all bands, so that the minimum value is 0. For site 2, because all values were positive and very consistent with the reference within the range of standard error, we used them in their original form for the MBI calculation. For site 3, given the relatively high uncertainty of k_b'/n (Fig. 4f), we decided not to use them but used the values in the neighboring site 2 instead.

3.2. Calculation of the MBI

Fig. 5 compares the original Hyperion true color images with the resulting MBI images with their corresponding color band assignments (red: Band 30; green: Band 21; blue: Band 15). The original true color image suffers from alternation of the apparent color and brightness caused by the water depth. The most typical area was found at site 2 (from the beach to the water channel containing the coral reef), which was corrected and expressed as a homogeneous light-blue color in the MBI image. This helps us focus on spectral

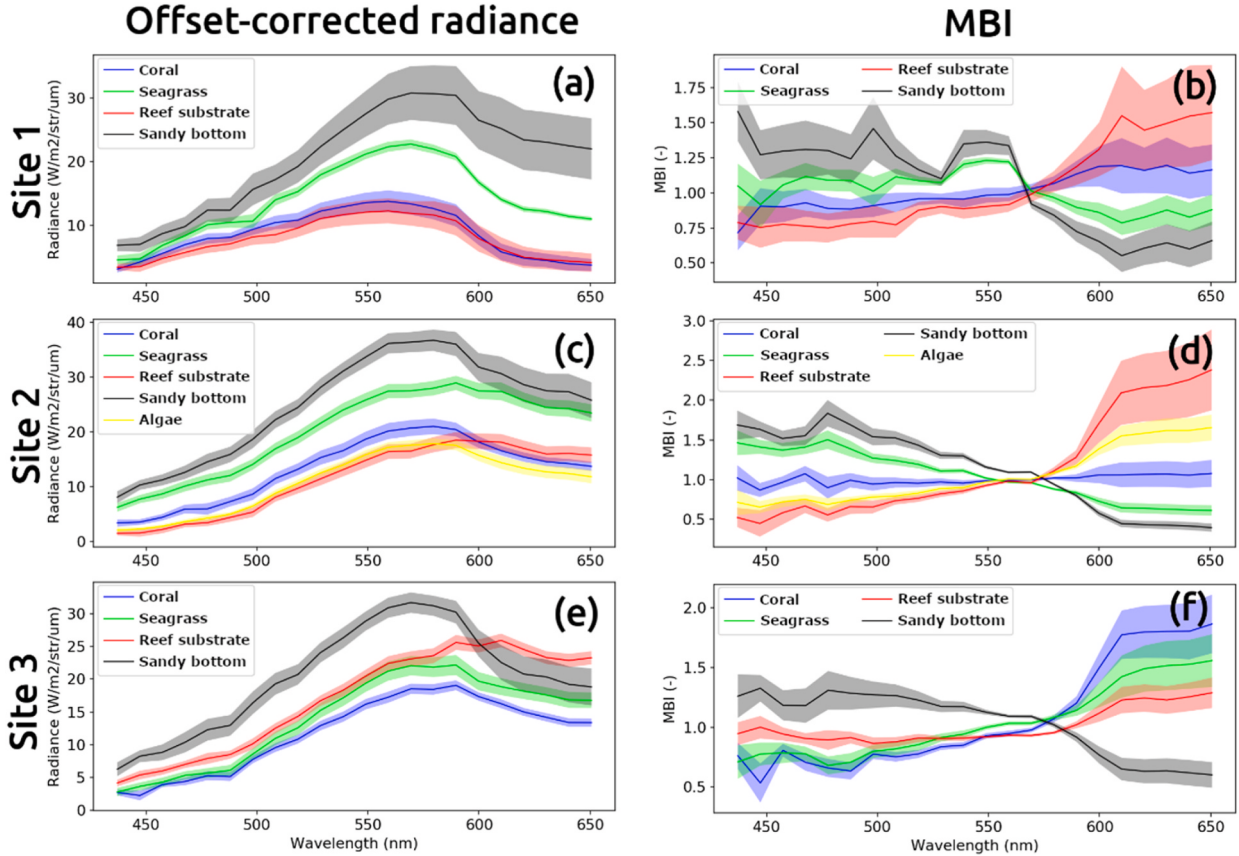


Fig. 6. Comparison of the offset-corrected radiance (i.e., $D_{i,b}$) and MBI spectra for each site. The solid lines in the offset-corrected radiance and MBI are the arithmetic and geometric means of each category, respectively. Shading represents the standard error (sample size of 10). Color correspondence for each category is the same as reference points in Fig. 5. (For interpretation of the references to color in this figure legend, the reader is referred to the Web version of this article.)

features of the benthic cover without water-column interference.

The variety of enhanced colors is likely to describe the benthic cover distribution. Compared with the benthic cover reference, the light blue may correspond to sandy bottom, yellow-green along the shoreline may correspond to seagrass or algae, and red near the reef crest may correspond to reef substrate. Breaking waves at the reef crest (typically at site 3) can be observed as a blue color. The color of the “coral” category seems to vary among sites. This is understandable because the density of the coral community differs greatly among the sites (and even within a site). The orange color at the middle of the reef flat area corresponds to the dense coral community observed at site 3. Sparse coral, typically distributed at site 1, should be observed as a mixture of pure coral and background material (usually sandy bottom), corresponding to a blue-green color.

The “spectrum” for each benthic cover category is shown in Fig. 6. The offset-corrected radiance (i.e., $D_{b,b}$) showed a similar spectral shape regardless of the category: a monotonic increase from 450 to 550 nm, a peak around 570 nm, and a decrease from 600 nm. The brightest target (i.e., the target having the highest radiance) was sandy bottom for all the sites, but the order of the other categories was not fixed. This is natural because categories at some sites are distributed in shallow areas, while they are in deep areas at other sites. The water column decreases the apparent radiance along the water depth, making it difficult to classify the categories solely with the brightness. As shown in the large uncertainty of the sandy bottom category at site 1, the apparent radiance largely fluctuated even in one category when the category is distributed over a wide range of water depth.

In contrast, the MBI showed better separability than the original radiance spectra. Mathematically, the average spectrum of all the available pixels for MBI calculation is constant (1.0). Reflecting the dominant category of each site, the standard spectrum (MBI = 1.0) changed, and the MBI spectral shape also changed. For sites 1 and 2, the dominant spectra were similar to the coral category, and thus the extracted MBI spectra of coral at the reference points were close to 1.0. For site 3, the extracted “coral” category (with high density) on the reference points does not represent the average for the site, and rather the “reef substrate” category (probably with a moderate density of living coral) does represent the average.

Generally speaking, the original (i.e., physical) reflectance spectra of the coral are weak at the blue wavelength region and rapidly increase in strength around 550–600 nm, with a peak around 600–650 nm (Hochberg et al., 2003). Compared with the pattern, the sandy bottom has a relatively flat physical reflectance spectrum. By taking the spectral shape for coral as the standard (MBI = 1.0), the MBI of the sandy bottom resulted in a contrasting shape: a high value in the blue wavelength region, followed by a rapid decrease around 550–600 nm, and a small value around 600–650 nm.

To interpret the spectral shape of the MBI more clearly, the geometric mean of the MBI for each category was divided by that for sandy bottom (Fig. 7a–c). This means that the standard spectrum (MBI = 1.0) was changed from the average of all pixels into the sandy bottom category. For reference, literature spectral data (based on in-situ survey) of seagrass, brown hermatypic coral, and seagrass

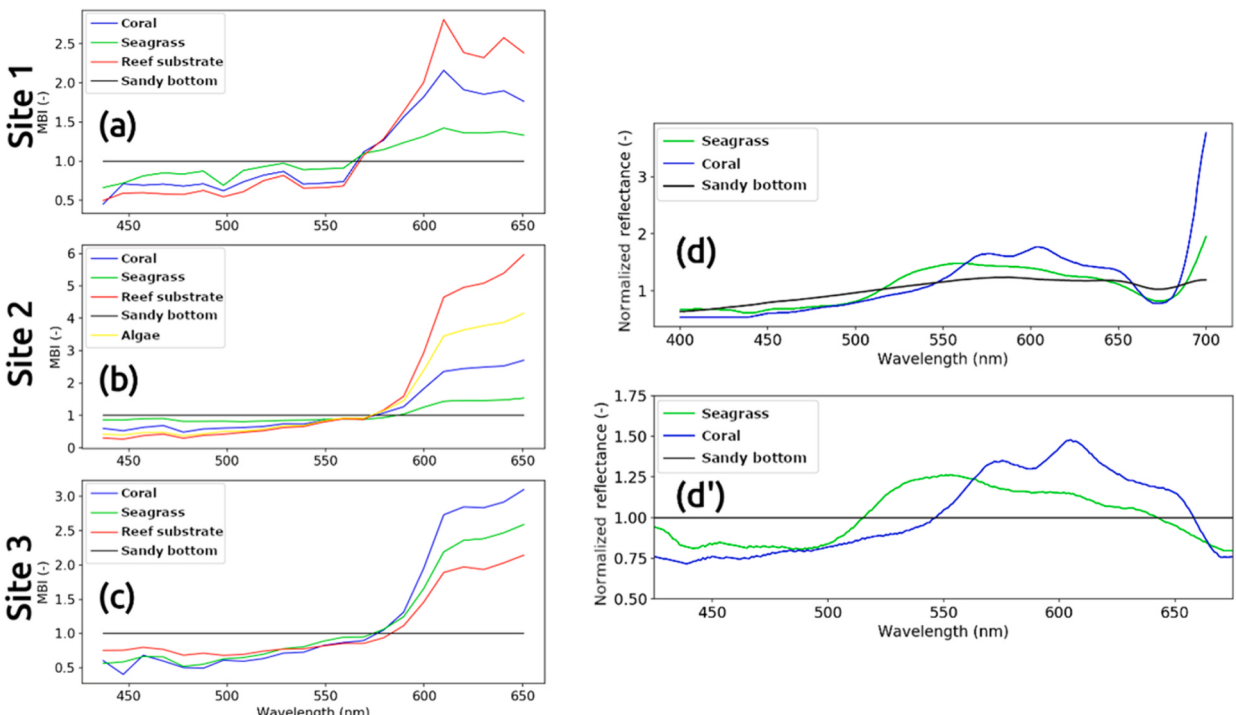


Fig. 7. MBI spectra standardized by the sandy bottom category for each site (a–c), and reference spectra for seagrass and coral (d, d'). (d) was modified from Hochberg et al. (2003) by scanning their graph of seagrass, brown hermatypic coral, and carbonate sand, and standardizing the results so that the geometric mean of all bands was 1.0. (d') was made by dividing all spectra by that of sandy bottom. The color correspondence for each category is the same as the Fig. 5 reference points. (For interpretation of the references to color in this figure legend, the reader is referred to the Web version of this article.)

were scanned from Hochberg et al. (2003); interpolated with a 1-nm interval; and standardized so that the geometric mean of all bands was 1.0 (Fig. 7d). Then, the spectrum for each category was divided by that of sandy bottom (Fig. 7d'), which should contain information equivalent to that in Fig. 7a–c. Spectra of the reef substrate are not shown, because they were not included in Hochberg et al. (2003). Those of algae are also not shown, because a wide variety of algae types were reported in Hochberg et al. (2003), and we could not tell which types of algae were distributed at site 2 based on MOEJ field survey data.

Comparison between coral and seagrass (Fig. 7a–c) showed consistency with the literature (Fig. 7d') to some extent. The best consistency of the spectral shape was observed at site 1: the seagrass signal was larger than the coral signal in the blue-green band region with a local minimum at 500 nm, followed by their reversal at around 570 nm, with a peak around 600 nm. The overall order between the two was also reasonable at sites 2 and 3 (seagrass > coral in the blue-green region and a reversal around 570 nm), but no clear peak pattern was observed for these sites. Even at site 1, the triple peaks at 570 nm, 600 nm, and 650 nm, which form the unique spectral pattern of the coral species, could not be clearly seen.

The order of reef substrate and coral was similar between sites 1 and 2, but different at site 3. This reflects the order of the original MBI, caused by the abovementioned difference in density of coral on the “coral” reference points. At sites 1 and 2, a relatively high density of living coral on the reef substrate should exaggerate the spectra of the “reef substrate” category over the “coral” category, and vice versa at site 3.

4. Discussion

We developed a new approach for shallow-water hyperspectral remote sensing that does not require inversion (Lee et al., 2001; Petit et al., 2017; Garcia et al., 2018; Minghelli et al., 2021) or explicit simulation (Yamano et al., 2002) of the radiative transfer process. It mitigates the water-column effect on the apparent radiance, and enhances the spectral patterns of bottom materials. The entire process can be implemented solely by using the hyperspectral image, without (1) a priori knowledge about the in-situ spectra of benthic cover, endmember types of the benthic cover, and bathymetry; (2) sophisticated atmospheric correction; or (3) non-trivial settings for inversion or forward simulation of shallow-water radiative transfer (although these methods would improve the results). This data-driven feature of the MBI approach is convenient for a wide range of users who want to quickly apply hyperspectral data to coastal monitoring.

We also confirmed that the MBI approach has advantages in hyperspectral data processing over the existing BI approach (Lyzenga 1978, 1981; Manessa et al., 2014), which is also a data-driven water-column correction method. The BI uses only two bands for estimation of the attenuation coefficient ratio, which suffers from correlation degradation between the two bands (Fig. 3; Table 2) and an explosion of combinatorial calculations for the large number of bands in hyperspectral data.

The differences in correlation degradation in the two-band scatterplots among sites (i.e., sites 1 and 3 showed lower correlation than site 2) can be attributed to imperfections in the selection of sample pixels and deep-water pixels, and/or heterogeneity in water and atmosphere for each site. Considering Eq. (4), the major factor affecting linearity between the two bands and estimation of k_{pq} can be separated into uncertainty in R and D . The heterogeneity in benthic cover of sampling pixels affects the uncertainty in R , and sites 1 and 3 may potentially contain heterogeneous benthic cover and more uncertainty in selection of homogeneous reference points that were expected to have the same benthic cover and the same reflectance R . Selection of deep-water pixels and sensor noise affects the uncertainty in D . If the L_{0b} values derived from deep-water pixels have no commonality with each shallow-water pixel, the calculated D value contains bias. At sites 1 and 3, spatial heterogeneity in the water surface and/or atmosphere may result in diverged D values in each sampling pixel. Sensor noise also affects D , especially when observing relatively deep areas and/or observing with long wavelengths, where only a small effective bottom signal exceeds the noise. The lower correlation for the red bands (Fig. 3; Table 2) can be explained by the lower signal-to-noise ratio. This is particularly the case for hyperspectral sensors that tend to have relatively low signal-to-noise ratio for one band in comparison to multispectral sensors (Moses et al., 2012). Differences in water depth and benthic cover reflectance among sites may result in different signal-to-noise ratios. In addition, deviation from the uniformity assumption—that is, k_b (relating to water properties) and E_b (relating to water and atmospheric properties) are uniform—also degrades the correlation. Spatial heterogeneity in the water and atmosphere even in the narrow region of interest can lead to uncertain k_{pq} estimation.

Our MBI approach robustly estimated the attenuation coefficient (Fig. 4; Table 3) and derived straightforward information (i.e., standardized spectra) by simultaneously using all effective bands in only a single calculation.

In the first stage of our MBI approach, estimation of the standardized attenuation coefficient k_b' derived a reasonable spectral pattern of k_b' for all the study sites: small attenuation in the blue wavelength region, an increase around the green region, and high attenuation in the red region. The same type of uncertainty should be included in D for k_b' calculation in the MBI algorithm [Eq. (9)], as for the k_{pq} calculation in the BI algorithm. However, by using all effective bands simultaneously and taking the double arithmetic mean of D for the spatial and spectral domains, and further taking the arithmetic mean of the multiple outputs of k_b' , the best available k_b' is likely to mitigate the uncertainty in each band. In general, neighboring bands in hyperspectral sensors show quite high correlation, but distant bands do not (Mizuuchi et al., 2020). The MBI approach can maintain the link between neighboring bands, and thus it is superior to direct comparison between two distant bands (i.e., the BI approach).

The important point for retrieving such a reasonable pattern was successful selection of the (1) reference pixels and (2) effective bands. From the viewpoint of (1), it is preferable that reference pixels be collected over a wide range of water depth. Uncertain estimation of k_b' at site 3 can be partly attributed to a smaller range of water depth in the selected reference pixels, because they were collected over a well-developed reef flat generally lacking deep water.

From the viewpoint of (2), our criteria—the effective bands where maximum radiance among deep-water pixels does not exceed the minimum radiance among reference pixels—were determined as Bands 9–30. This corresponds to the bands at 437–651 nm (see the

Appendix), covering a wide range of visible wavelengths. In the case study for site 1, adding longer wavelength bands (i.e., Bands 8–34) resulted in an unstable k_b' pattern (Fig. 4c), suggesting that the region with longer red wavelengths does not provide a sufficient signal and is not suited to benthic observation at the site. However, this longer red wavelength region (the so-called “red edge”) and even longer region (i.e., near infrared) also have valuable information about the status of coral (Yamano et al., 2003b) and water quality (Brando and Dekker, 2003), and thus may be needed for the purpose of ecological monitoring. In such cases, the literature values of k_b' (e.g., Hale and Querry, 1973; Smith and Baker, 1978) may alternatively be used for the MBI calculation for the longer-wavelength bands, although the derived MBI will have large uncertainty in the bands due to a low signal-to-noise ratio (for the bottom reflection).

In contrast, one may also use our approach to qualitatively infer the optical properties of water from the k_b' value. For example, the spectral pattern of k_b' at site 2 (Fig. 4e) was similar to that for pure water, rather than seawater, which is likely due to the inflow of fresh water from the Miyara River. The river inflow may also elevate the level of suspended or dissolved matter, as suggested by the slightly higher value in the short-wavelength region around 430–470 nm. Fig. 8 shows the simulated water attenuation coefficients obtained using the semi-analytical model (Lee et al., 1998) with the environmental parameters for clear ocean: chlorophyll *a* concentration = 0.5 mg/m³ and the gelbstoff and detritus absorption coefficients at 440 nm = 0.05 m⁻¹. In a “clear” ocean, seawater absorption dominantly determines the total attenuation; however, at short wavelengths, phytoplankton, gelbstoff, and detritus absorption also increases the total attenuation. This may suggest that site 2 contains more dissolved or suspended matter with more phytoplankton than at the other two sites, because of river inflow from an urban area.

The second stage of our MBI approach created MBI maps (Fig. 5) and MBI spectra (Fig. 6) for all available pixels over the reef flat, which enhanced the visibility and seemed to contain more information about the benthic cover than did the original radiance data, which were affected by water-column attenuation. The derived spectral pattern of the MBI improved the separability of each benthic cover, and was generally consistent with the in-situ spectra (Hochberg et al., 2003) of seagrass, coral, and sandy bottom (Fig. 7). The result suggests that MBI improves the accuracy of classification using hyperspectral imagery in the shallow benthic cover (Zhang, 2015), which will be an important future work.

Because the MBI is a standardized value so that (1) average spectra for all available pixels in the site can be monotonic (MBI = 1.0) and (2) the geometric mean of all effective bands for one pixel can be 1.0, it requires some technical effort to interpret the real (i.e., physical) reflectance spectra. From the viewpoint of (1), changing the standard spectra from the site average into some grey target having real monotone spectra (Tsuchida et al., 1992) makes the MBI spectral shape similar to the real one. As we did in Fig. 7, the sandy bottom may be useable as a quasi-grey target.

From the viewpoint of (2), ancillary information about the real broadband albedo of the target is likely needed to translate the MBI spectral pattern into absolute reflectance. The absolute reflectance value may be required for physical modeling, including a description of the energy budget, which will also be future work.

The case study with EO-1 Hyperion data did not seem to achieve sufficient accuracy for sophisticated applications, such as spectral pattern analysis (Yamano et al., 2002; Hochberg and Atkinson, 2000) and quantitative estimation of water optical properties (Brando and Dekker, 2003). Sophisticated pre-processing, including inter-band calibration (Mizuuchi et al., 2020) and atmospheric correction (Gao et al., 2009; Vahtmae and Kutser, 2013) would improve the accuracy. Study with recent hyperspectral satellite sensors, such as HISUI (Matsunaga et al., 2018), DESIS (Alonso et al., 2019), and PRISMA (Vangi et al., 2021), is also an attractive avenue for analysis with a better signal-to-noise ratio. One more advantage of using recently commissioned sensors is that an in-situ ground reference can be newly collected. The proxy reference data for benthic cover categories used in this research are likely to have uncertainty arising from a temporal gap between the field survey (MOEJ, 1991; 2018) and the satellite observation, and a mixture of pure endmembers within one Hyperion pixel. Application to recent hyperspectral sensors with a more reliable ground reference is expected to demonstrate the usefulness of the MBI approach more clearly.

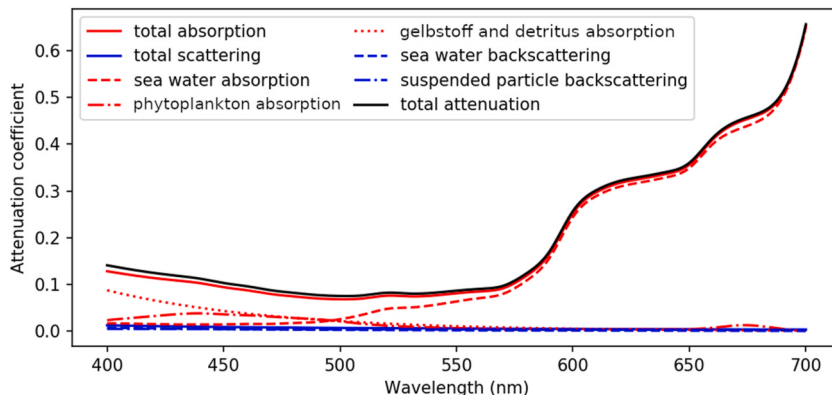


Fig. 8. Simulation of water attenuation coefficients using the semi-analytical model (Lee et al., 1998). Different sources of attenuation were separately simulated and added.

5. Conclusion

This study developed a new method for shallow-water hyperspectral remote sensing, named the MBI approach. It does not require non-trivial settings of radiative transfer simulation or inversion, and it is useful for enhancing the spectral patterns of benthic materials, while mitigating the influence of the water column on the apparent radiance. The MBI approach incorporates the empirical radiative transfer theory developed by [Lyzenga \(1978\)](#), called the BI approach. However, the MBI approach is more suited for hyperspectral data than the existing BI approach because it simultaneously uses all effective bands to derive the standardized water attenuation coefficient and MBI. A case study with actual hyperspectral satellite data (Hyperion) revealed that the MBI approach has more robust performance in the estimation of the water attenuation coefficient than does the existing BI approach. The derived MBI map successfully enhanced the spectral pattern of benthic materials, and the overall spectral pattern of MBI for available categories (i.e., seagrass, coral, and sandy bottom) at Ishigaki Island near Okinawa, Japan, was consistent with the patterns published in the literature. The MBI method is promising for application to data from recently commissioned hyperspectral satellite sensors for water quality estimation, more sophisticated spectral analysis, and classification of the benthic cover communities.

Funding sources

This research was supported by Research Laboratory on Environmentally-conscious Developments and Technologies (E-code) of the National Institute of Advanced Industrial Science and Technology, and also supported by the Ministry of Economy, Trade and Industry of Japan.

Ethical Statement

Hereby, we (Hiroki Mizuuchi, Satoshi Tsuchida, Masaru Mizuyama, Satoru Yamamoto, Koki Iwao) consciously assure that for the manuscript "Multi-band bottom index: a novel approach for coastal environmental monitoring using hyperspectral data" the following is fulfilled:

- 1) This material is the authors' own original work, which has not been previously published elsewhere.
- 2) The paper is not currently being considered for publication elsewhere.
- 3) The paper reflects the authors' own research and analysis in a truthful and complete manner.
- 4) The paper properly credits the meaningful contributions of co-authors and co-researchers.
- 5) The results are appropriately placed in the context of prior and existing research.
- 6) All sources used are properly disclosed (correct citation). Literally copying of text must be indicated as such by using quotation marks and giving proper reference.
- 7) All authors have been personally and actively involved in substantial work leading to the paper, and will take public responsibility for its content.

We agree with the above statements and declare that this submission follows the policies of Remote Sensing Applications: Society and Environment as outlined in the Guide for Authors and in the Ethical Statement.

Author statement

Conceptualization, H.M. and S.T.; data curation, H.M. and M.M.; formal analysis, H.M.; investigation, H.M.; Methodology, H.M. and S.T.; project administration, S.Y. and K.I.; Validation, H.M.; Visualization, H.M.; Writing – original draft, H.M.; Writing – review and editing, S.T., M.M., S.Y. and K.I.

Declaration of competing interest

The authors declare that they have no known competing financial interests or personal relationships that could appear to influence the work reported in this paper.

Appendix. Correspondence between Hyperion band number and wavelength in the visible and near-infrared spectral region

Band number	Wavelength (nm)	Band number	Wavelength (nm)
8	426.82	33	681.20
9	436.99	34	691.37
10	447.17	35	701.55
11	457.34	36	711.72
12	467.52	37	721.90
13	477.69	38	732.07
14	487.87	39	742.25
15	498.04	40	752.43
16	508.22	41	762.60

(continued on next page)

(continued)

Band number	Wavelength (nm)	Band number	Wavelength (nm)
17	518.39	42	772.78
18	528.57	43	782.95
19	538.74	44	793.13
20	548.92	45	803.30
21	559.09	46	813.48
22	569.27	47	823.65
23	579.45	48	833.83
24	589.62	49	844.00
25	599.80	50	854.18
26	609.97	51	864.35
27	620.15	52	874.53
28	630.32	53	884.70
29	640.50	54	894.88
30	650.67	55	905.05
31	660.85	56	915.23
32	671.02	57	925.41

References

- Alonso, K., Bachmann, M., Burch, K., Carmona, E., Cerra, D., de los Reyes, R., Dietrich, D., Heiden, U., Holderlin, A., Ickes, J., et al., 2019. Data products, quality and validation of the DLR earth sensing imaging spectrometer (DESI). *Sensors* 19, 4471.
- Andrefouet, S., Kramer, P., Torres-Pulliza, D., Joyce, K.E., Hochberg, E.J., Garza-Perez, R., Mumby, P.J., Riegl, B., Yamano, H., White, W.H., Zubia, M., Brock, J.C., Phinn, S.R., Naseer, A., Hatcher, B.G., Muller-Karger, F.E., 2003. Multi-site evaluation of IKONOS data for classification of tropical coral reef environments. *Remote Sens. Environ.* 88, 128–143.
- Arabi, B., Salama, M.S., van der Wal, D., Pitarch, J., Verhoef, W., 2020. The impact of sea bottom effects on the retrieval of water constituent concentrations from MERIS and OLCI images in shallow tidal waters supported by radiative transfer modeling. *Remote Sens. Environ.* 237, 111596.
- Barnes, B.B., Hu, C., Schaeffer, B.A., Lee, Z., Palandro, D.A., Lehrter, J.C., 2013. MODIS-derived spatiotemporal water clarity patterns in optically shallow Florida Keys waters: a new approach to remove bottom contamination. *Remote Sens. Environ.* 134, 377–391.
- Brando, V.E., Dekker, A.G., 2003. Satellite hyperspectral remote sensing for estimating estuarine and coastal water quality. *IEEE Trans. Geosci. Rem. Sens.* 41 (6), 1378–1387.
- Burke, L., Reytar, K., Spalding, M., Perry, A., 2011. Reefs at Risk Revisited. World Resources Institute Washington. Available at: https://files.wri.org/d8/s3fs-public/pdf/reefs_at_risk_revisited.pdf. (Accessed 13 December 2021).
- Campbell, P.K.E., Middleton, E.M., Thome, K.J., Kokaly, R.F., Huemmrich, K.F., Lagomasino, D., Novick, K.A., Brunsell, N.A., 2013. EO-1 Hyperion reflectance time series at calibration and validation sites: stability and sensitivity to seasonal dynamics. *IEEE J-STARS*. 6, 276–290.
- Garcia, R.A., Lee, Z., Hochberg, E.J., 2018. Hyperspectral shallow-water remote sensing with an enhanced benthic classifier. *Rem. Sens.* 10, 147.
- Garcia, R.A., Lee, Z., Barnes, B.B., Hu, C., Dierssen, H.M., Hochberg, E.J., 2020. Benthic classification and IOP retrievals in shallow water environments using MERIS imagery. *Remote Sens. Environ.* 249, 112015.
- Green, A.A., Craig, M.D., 1985. In: Analysis of Aircraft Spectrometer Data with Logarithmic Residuals. Proceedings of the Airborne Imaging Spectrometer Data Analysis Workshop. Jet Propulsion Laboratory, pp. 111–119.
- Hale, G.M., Querry, M.R., 1973. Optical constants of water in the 200-nm to 200-μm wavelength region. *Appl. Opt.* 12 (3), 555–563.
- Hasegawa, H., Yamano, H., 2004. Yaeyama archipelago, Ishigaki island. Coral reefs of Japan. In: The Japanese Coral Reef Society and Ministry of the Environment, p. 220.
- Hedley, J.D., Mobley, C.D., 2019. HydroLight 6.0 Ecolight 6.0 Users' Guide. Numerical Optics Ltd. Available at: <https://www.numopt.com/doc/HE60UsersGuide.pdf>. (Accessed 13 December 2021).
- Hedley, J.D., Roelfsema, C.M., Chollett, I., Harborne, A.R., Heron, S.F., Weeks, S., Skirving, W.J., Strong, A.E., Eakin, C.M., Christensen, T.R.L., Ticzon, V., Bejarano, S., Mumby, P.J., 2016. Remote sensing of coral reefs for monitoring and management: a review. *Rem. Sens.* 8 (2), 118.
- Hochberg, E.J., Atkinson, M.J., 2000. Spectral discrimination of coral reef benthic communities. *Coral Reefs* 19, 164–171.
- Hochberg, E.J., Atkinson, M.J., Andrefouet, S., 2003. Spectral reflectance of coral reef bottom-types worldwide and implications for coral reef remote sensing. *Remote Sens. Environ.* 85, 159–173.
- Kanno, A., Tanaka, Y., 2012. Modified Lyzenga's method for estimating generalized coefficients of satellite-based predictor of shallow water depth. *Geosci. Rem. Sens. Lett. IEEE* 9 (4), 715–719.
- Kayanne, H., Harii, S., Ide, Y., Akimoto, F., 2002. Recovery of coral populations after the 1998 bleaching on shiraho reef, in the southern ryukyus, NW pacific. *Mar. Ecol. Prog. Ser.* 239, 93–103.
- Lee, Z., Carder, K.L., Mobley, C.D., Steward, R.G., Patch, J.S., 1998. Hyperspectral remote sensing for shallow waters: I. A semianalytical model. *Appl. Opt.* 37 (27), 6329–6338.
- Lee, Z., Carder, K.L., Mobley, C.D., Steward, R.G., Patch, J.S., 1999. Hyperspectral remote sensing for shallow waters: II. Deriving bottom depths and water properties by optimization. *Appl. Opt.* 38 (18), 3831–3843.
- Lee, Z., Carder, K.L., Chen, R.F., Peacock, T.G., 2001. Properties of the water column and bottom derived from airborne visible infrared imaging spectrometer (AVIRIS) data. *J. Geophys. Res.* 106 (C6), 11639–11651.
- Liu, G., Heron, S.F., Eakin, C.M., Muller-Karger, F.E., Vega-Rodriguez, M., Guild, L.S., de la Cour, J.L., Geiger, E.F., Skirving, W.J., Burgess, T.F.R., Strong, A.E., Harris, A., Maturi, E., Ignatov, A., Sapper, J., Li, J., Lynds, S., 2014. Reef-scale thermal stress monitoring of coral ecosystems: new 5-km global products from NOAA coral reef watch. *Rem. Sens.* 6 (11), 11579–11606.
- Lyzenga, D.R., 1978. Passive remote sensing techniques for mapping water depth and bottom features. *Appl. Opt.* 17 (3), 379–383.
- Lyzenga, D.R., 1981. Remote sensing of bottom reflectance and water attenuation parameters in shallow water using aircraft and Landsat data. *Int. J. Rem. Sens.* 2 (1), 71–82.
- Lyzenga, D.R., Malinas, N.P., Tanis, F.J., 2006. Multispectral bathymetry using a simple physically based algorithm. *IEEE Trans. Geosci. Rem. Sens.* 44 (8), 2251–2259.
- Manessa, M.D.M., Kanno, A., Sekine, M., Ampou, E.E., Widagti, N., As-syakur, A.R., 2014. Shallow-water benthic identification using multispectral satellite imagery: investigation on the effects of improving noise correction method and spectral cover. *Rem. Sens.* 6, 4454–4472.
- Matsunaga, T., Hoyano, A., Mizukami, Y., 2001. Monitoring of coral reefs on Ishigaki Island in Japan using multitemporal remote sensing data. *Proc. SPIE* 4154, 212–222.

- Matsunaga, T., Iwasaki, A., Tsuchida, S., Iwao, K., Nakamura, R., Yamamoto, H., Kato, S., Obata, K., Kashimura, O., Tanii, J., et al., 2018. HISUI status toward FY2019 launch. In: Proceedings of 2018 International Geoscience and Remote Sensing Symposium. IGARSS), Valencia, Spain, pp. 160–163, 22–27 July 2018.
- McCarthy, M.J., Colna, K.E., El-Mezayen, M.M., Laureano-Rosario, A.E., Mendez-Lazaro, P., Otis, D.B., Toro-Farmer, G., Vega-Rodriguez, M., Muller-Karger, F.E., 2017. Satellite remote sensing for coastal management: a review of successful applications. Environ. Manag. 60, 323–339.
- Ministry of the Environment, Biodiversity Center of Japan, 1991. Marine Biotic Survey (Coral Reef Survey), in the 4th National Survey on the Natural Environment. [in Japanese] available at: http://www.biodic.go.jp/reports2/4th/coralreef/4_coralreef.pdf. (Accessed 10 December 2021).
- Ministry of the Environment, Biodiversity Center of Japan, 2018. Survey on current situation of the coastal ecosystem for climate change initiative [in Japanese] available at: https://www.biodic.go.jp/kiso/44/reports/h29_kikou_houkoku.pdf. (Accessed 16 December 2021).
- Miura, M., Sakai, S., Aoyama, S., Ishii, J., Ito, K., Aoki, T., 2012. High-accuracy image matching using phase-only correlation and its application. In: 2012 Proceedings of SICE Annual Conference (SICE), pp. 307–312.
- Mizuochi, H., Tsuchida, S., Obata, K., Yamamoto, H., Yamamoto, S., 2020. Combination of cross- and inter-band radiometric calibrations for a hyperspectral sensor using model-based band adjustment. Rem. Sens. 12 (12), 2011.
- Moses, W.J., Bowles, J.H., Lucke, R.L., Corson, M.R., 2012. Impact of signal-to-noise ratio in a hyperspectral sensor on the accuracy of biophysical parameter estimation in case II water. Opt Express 20 (4), 4309–4330.
- Nadaoka, K., Paringit, E.C., Yamano, H., 2004. Remote sensing of coral reefs in Japan. Coral Reefs of Japan. In: The Japanese Coral Reef Society and Ministry of the Environment, p. 89.
- Petit, T., Bajjouk, T., Mouquet, P., Rochette, S., Vozel, B., Delacourt, C., 2017. Hyperspectral remote sensing of coral reefs by semi-analytical model inversion – comparison of different inversion setups. Remote Sens. Environ. 190, 348–365.
- Smith, R.C., Baker, K.S., 1978. Optical classification of natural waters. Limnol. Oceanogr. 23 (2), 260–267.
- Sochea, L., Sakuno, Y., 2008. Eelgrass bed monitoring using satellite TERRA/ASTER data in Yoshida tidal flat. Processings of Hydraulic Engineering 52, 1381–1386 ([in Japanese]).
- Tsuchida, S., Odajima, T., Tanaka, S., 1992. Gray scale log residual method for reflectance pattern analysis. Journal of the Remote Sensing Society of Japan 12 (3), 29–43 ([in Japanese]).
- Tsuchida, S., Tanaka, S., Odajima, T., 1993. Spectral pattern index for logarithmic residual and the similar methods. J. Jpn. Soc. Photogrammetry 32 (1), 25–35 ([in Japanese]).
- Ungar, S.G., Pearlman, J.S., Mendenhall, J.A., Reuter, D., 2003. Overview of the earth observing one (EO-1) mission. IEEE Trans. Geosci. Rem. Sens. 41, 1149–1159.
- USGS, 2018. USGS EROS Archive – Landsat Archives – Landsat 7 Enhanced Thematic Mapper Plus (ETM+) Level-1 Data Products. <https://doi.org/10.5066/F7WH2P8G>. (Accessed 5 January 2022).
- Vangi, E., D'Amico, D., Francini, S., Giannetti, F., Lasserre, B., Marchetti, M., Chirici, G., 2021. The new hyperspectral satellite PRISMA: imagery for forest types discrimination. Sensors 21, 1182.
- Vahtmae, E., Kuusar, T., 2013. Classifying the Baltic Sea shallow water habitats using image based and spectral library methods. Rem. Sens. 5, 2451–2474.
- Yamano, H., Tamura, M., Kunii, Y., Hidaka, M., 2002. Hyperspectral remote sensing and radiative transfer simulation as a tool for monitoring coral reef health. Mar. Technol. Soc. J. 36 (1), 4–13.
- Yamano, H., Abe, O., Matsumoto, E., Kayanne, H., Yonekura, N., 2003a. Influence of wave energy on Holocene coral reef development: an example from Ishigaki Island, Ryukyu Islands, Japan. Sediment. Geol. 159, 27–41.
- Yamano, H., Tamura, M., Kunii, Y., Hidaka, M., 2003b. Spectral reflectance as a potential tool for detecting stressed corals. Galaxea JCRS 5, 1–10.
- Yamano, H., Tamura, M., 2004. Detection limits of coral reef bleaching by satellite remote sensing: simulation and data analysis. Remote Sens. Environ. 90, 86–103.
- Zhang, C., 2015. Applying data fusion techniques for benthic habitat mapping and monitoring in a coral reef ecosystem. ISPRS J. Photogrammetry Remote Sens. 104, 213–223.
- Zoffoli, M.L., Frouin, R., Kampel, M., 2014. Water column correction for coral reef studies by remote sensing. Rem. Sens. 14, 16881–16931.